Materials Research Proceedings 28 (2023) 445-454 https://doi.org/10.21741/9781644902479-49

Chevron cracking during full forward impact extrusion of aluminum alloy EN AW 7075 in dependence of heat treatment condition and tribological system

MÜLLER Martina[1,a], SCHWARK Niklas[1,b*], WEISER Ingo F.[1,c], HERRIG Tim[1] and BERGS Thomas[1,2,d]

[1]Laboratory for Machine Tools and Production Engineering (WZL) of RWTH Aachen University, Campus-Boulevard 30, 52074 Aachen, Germany

[2]Fraunhofer Institute for Production Technology IPT, Steinbachstr. 17, 52074 Aachen, Germany

[a]martina.mueller@wzl.rwth-aachen.de, [b]N.Schwark@wzl.rwth-aachen.de, [c]I.Weiser@wzl.rwth-aachen.de, [d]t.bergs@wzl.rwth-aachen.de

Keywords: Aluminum, Full Forward Impact Extrusion, Chevron Cracking, Heat Treatment

Abstract. In addition to the growing demand for energy efficiency, the current and future legal emission limits in the transport sector lead to an increasing demand for weight-reduced components. By substituting conventional materials with weight-reduced components, such as the aluminum alloy EN AW 7075 (AlZn5.5MgCu), emissions during vehicle service life can be reduced. Chevron cracks, also called internal cracks, can be caused by a variety of reasons during cold extrusion processes and pose a great, non-visible challenge for product quality [1]. However, the cause effect relations between the heat treatment condition and the tribological system in regard to damage development have not yet been sufficiently analyzed. In order to examine these relations, the first forming step of a ball pivot was investigated using full forward impact extrusion. Experiments with different tribological systems were investigated by varying lubricant and die treatment with regard to friction and wear reduction. In addition, the effect of the workpiece formability on crack formation was examined by comparing the T6 and soft annealed state of EN AW 7075 as workpiece materials. During this study, the microstructure of both conditions was investigated to highlight differences. A validated FE process simulation using the simulation software Forge NxT 3.2 accompanied the process in order to evaluate the stress state during the full forward impact extrusion process and its relation to the occurrence of chevron crack formation. In the experiments conducted during this study, chevron cracking occurred during full forward impact extrusion of EN AW 7075 in state T6, while in soft annealed condition none appeared. Unlike the heat treatment condition, the tribological system had no impact on the occurrence of chevron cracking but on the severity of the cracks.

Introduction

The cold impact extrusion (CIE) process is an established, resource saving manufacturing process. CIE plays an important role in the cost-effective production of complex and ready-to-install components that are produced in large quantities. There is a large spectrum of possible component geometries that can be produced by CIE. Those are used in a wide range of applications, especially in the automotive industry [2]. Due to a growing demand for the CIE of high-strength products with lightweight properties, especially the production of parts using higher priced, lightweight materials like aluminum alloys becomes increasingly attractive. In many cases, the process limits of forming technologies, which are primarily determined by the material formability [3], are already exploited to their maximum. Exceeding the material formability limit can result in workpiece defects. These defects occur as surface or internal cracks, also called chevron cracks or

Materials Research Proceedings 28 (2023) 445-454 https://doi.org/10.21741/9781644902479-49

central bursting. While surface cracks can be easily and quickly detected, as they can be seen by visual inspection, chevron cracks pose a much greater challenge for product quality [1]. Thus, the topic of chevron cracking has been part of many studies in recent years, and a variety of reasons was presented for the occurrence of these defects during the extrusion process. McVeigh and Liu showed that low friction between workpiece and tool leads to the increased occurrence of chevron cracking since the hydrodynamic stress increases with decreased friction [4]. In addition, unsuitable material hardening behavior [4], hard, brittle microstructural phases or non-metallic inclusions [3], as well as unsuitable or improper heat treatments of the workpieces [5] can lead to an increased occurrence of chevron cracks. As follows from McAllen et al. [6], different geometrical properties of the reduction die, for example larger shoulder angles, can also cause defects in form of surface and chevron cracks. However, the correlation between the tribological system (TS) and the occurrence of chevron cracks has not yet been sufficiently analyzed.

Consequently, the aim of this work is to investigate this correlation by determining the material behavior of aluminum alloy EN AW 7075 during full forward impact extrusion (FFIE), which is a process variant of CIE, in order to avoid chevron cracking. FFIE experiments with two different heat treatment conditions (T6 and soft annealed), three different lubricants and three different reduction die treatments were performed and subsequently analyzed in order to investigate the cause effect relations between these parameters and the occurrence of chevron cracking. All experiments were repeated three times to increase statistical value. The experiments were performed using a full factorial design.

Methods, Machines and Materials

Workpiece, tool material and experimental setup.

The experiments were conducted using full forward impact extrusion. The tools for the full forward impact extrusion, which consist of a punch, reduction die and shaft die, are shown in Fig. 1 (b). As tool material, high speed steel HS 6-5-2C (material number 1.3334) as well as the carbon steel G52 (no AISI equivalent) were used and hardened to 62 HRC. The reduction dies were provided with a shoulder opening angle of $\alpha = 45°$, had an initial diameter of $d_a = 31.4$ mm and a taper diameter of $d_{i1} = 20.6$ mm, see Fig. 1 (b). In order to prevent the sample from clinging to the inner wall of the die after taper, a heel was provided to increase the diameter to $d_{i2} = 20.7$ mm.

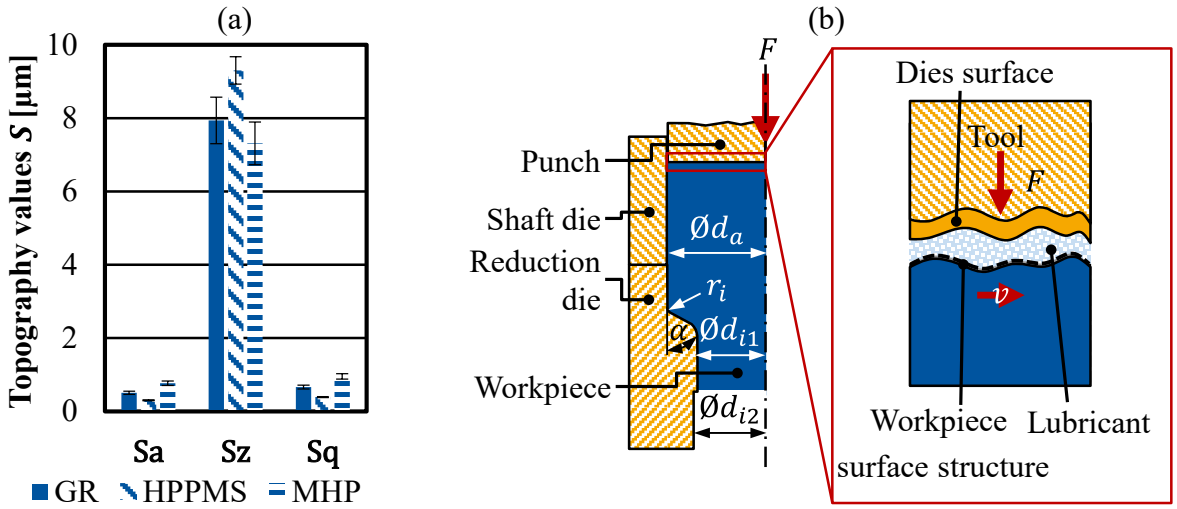

Fig. 1. Topography values of the dies according to ISO 25178 (a) and schematic illustration of the used tools (b).

The reduction die surfaces were finished by means of three different treatments. The first die was provided with a CrAlN-MoSx coating using high power pulsed magnetron sputtering (HPPMS) and were subsequently polished (Rz = 1 µm). The second die was processed by machine hammer peening (MHP) in order to increase wear resistance due to residual compressive stresses and to form lubricant pockets at the same time. The last die was ground (GR) after the manufacturing process. After treatment, the surface roughness was measured according to DIN EN ISO 25178 using a combined roughness and contour measurement system Hommel Etamic nanoscan 855 by Jenoptik AG. The results of these measurements are shown in Fig. 1 (a).

The experiments were carried out using the Schuler AG hydraulic press HPX-400. The press has a maximum pressing force of F_{max} = 4000 kN and was adjusted to a constant velocity of v = 12 mm/s. The punch path was kept constant at s = 12 mm. The results were partly evaluated using statistical methods of Design of Experiments (DoE), including main effects calculation. For DoE, adjustable parameters, also called factors, and their settings are determined, while the other process parameters remain constant. During the experiments, all combinations between the settings of the adjustable parameters are tested [8]. As adjustable parameters, die treatment (A) and lubricant (B) were chosen.

As workpiece material, the aluminum alloy EN AW 7075 was used, which is a widely used material for cold forming processes [7]. It is a hardenable wrought alloy, which provides high to highest static strength properties [6]. In order to transfer the material from the T6 condition to the soft annealed condition, the material was heat treated, see Fig. 2 (a). As can be seen in Fig. 2 (b-c), the texture was reshaped and showed a finer appearance in the soft annealed state. Before and after the treatment, microsections were etched using nitric acid n_{HNO_3}, hydrochloric acid n_{HCl}, hydrofluoric acid n_{HF} and water n_{H_2O}. Before the experiments were conducted, all workpieces were turned, ground and then shot-peened with aluminum granulate to improve lubricant bonding.

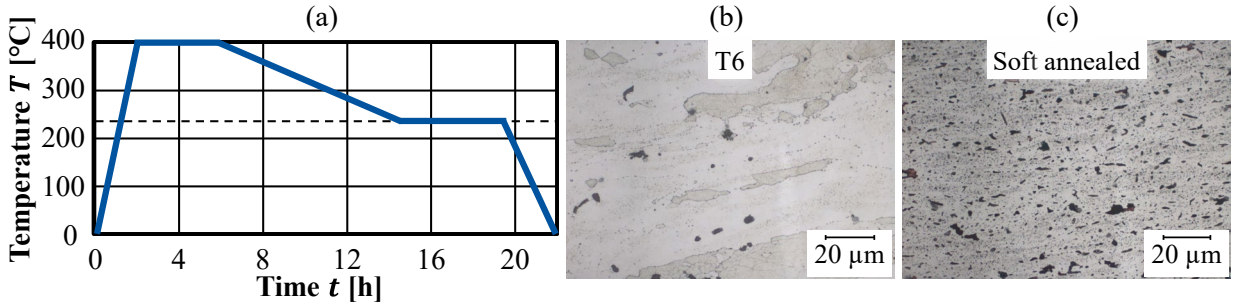

Fig. 2. Time table of heat treatment (a) and microsections of heat treatment condition T6 (b) and soft annealed (c).

Three different dry lubricants were applied on the workpieces. The application was carried out according to the recommendations of the lubricant manufacturer. The first lubricant (S1) was a water-soluble, low-dust lubricant for dry or wet treatment of aluminum workpieces prior to forming. It is used as an alternative to zinc stearate powder and wax systems. The lubricant was dissolved in distilled water with a solid content of 20 g/l and afterwards applied on the workpieces using a lubricant bath. The second lubricant (S2) was an aqueous polymer dispersion with a solid content of 20.5%, which forms a transparent, non-slip film and was applied on the workpieces using a lubricant bath with a 35% concentration. The third lubricant (S3) was an aqueous suspension of solid lubricants with a solid content of 26%. It was applied using a lubricant bath with a 45% concentration.

Numerical setup.

The experiments were accompanied by a finite elements (FE) simulation model using Forge NxT 3.2. The workpiece was modelled as an elasto-plastic, deformable volume. The punch and die were assumed to be rigid, non-deformable bodies. To reduce the required computing power and the calculation time, only one twelfth of the rotationally symmetrical components was implemented, see Fig. 3 (a). In post processing, these components were combined in order to analyze the complete workpiece. The velocity of the punch v as well as the punch path s were set to $v = 12$ mm/s and $s = 12$ mm to reflect the conditions of the experiments. For modelling the friction, a coupled friction model as a combination of Tresca's and Coulomb's friction models was used, see Fig. 3 (b).

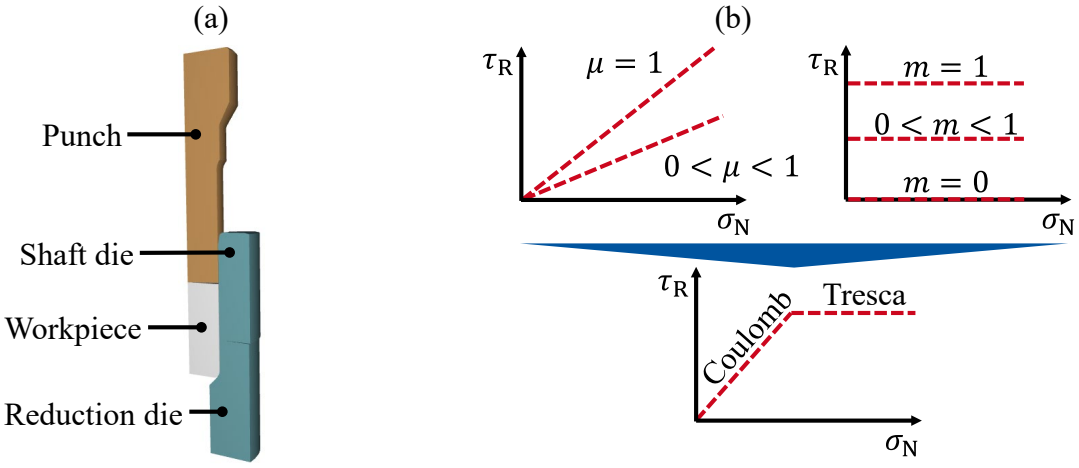

Fig. 3. Image of simulation model (a) and used friction model (b).

In order to represent various tribological conditions during forming, different coefficients of friction μ and friction factors m were used during the simulations. These are listed in Table 1.

Table 1. Coefficients of friction μ and friction factors m of implemented frictions laws.

Description	**Coefficients of friction μ / friction factors m**
Low friction	0.02 / 0.05
High friction	0.2 / 0.4

The meshing was carried out with the triangulation method, in which the geometry of the components was simulated using triangular facets. In order to reduce the calculation complexity on the one hand and to lower the error level on the other hand, a convergence analysis was carried out. Starting from a coarse mesh, the elements were reduced in size until the results of the simulation (punch force, stress distribution) converged. The mesh determined by the convergence analysis defined the edge length to a minimum mesh size of l_{min} = 0.02 mm.

Experimental and Numerical Results

Experimental results.

The diagram in Fig. 4 (a) displays the punch force-time-graphs of the first stroke of the different test pairings. Comparing the graphs reveals a similar course of each test pairing. At first, the punch force F increased quadratically until a linear progression was established, which continued until the maximum punch force F_{max} was achieved. With the exception of the TS that is induced by

HPPMS and S1, the gradient of the punch force-time-graphs reached a continuous, decreasing negative value after reaching the maximum punch force F_{max} and before the end of the FFIE process where the punch force F dropped to F = 0 kN. However, in the course of the TS consisting of HPPMS and S1, the gradient of the punch force-time-graph underwent a change of sign after reaching the maximum punch force F_{max}. The punch force F increased to a local maximum before the end of the FFIE process. The drop in the force curve can be explained by sudden stress relief after the occurrence of a chevron crack. Besides the similar course of each punch force-time-graph, different maximum punch forces F_{max} were achieved in each experiment. The highest punch force F_{max} = 751 kN was achieved by using S3 and the HPPMS treated die. The use of the HPPMS treated die and S1 required the lowest punch force F_{min} = 619 kN. The punch force F did not increase or decrease systematically with increasing stroke number. Thus, wear effects that occurred during this study can supposedly be neglected.

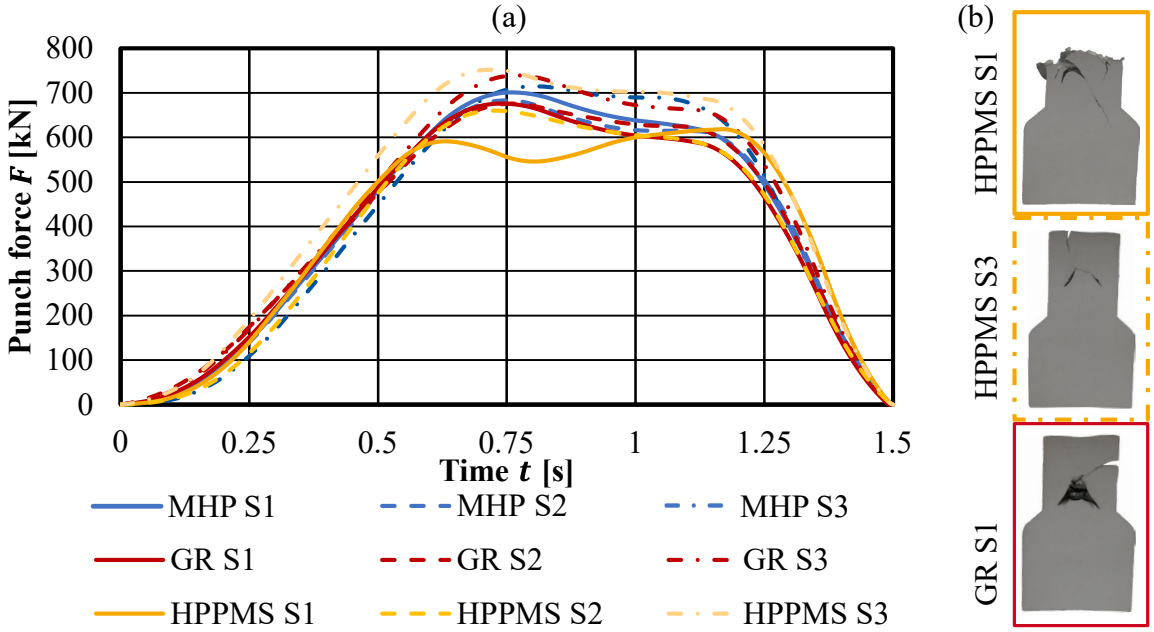

Fig. 4. Punch force-time-diagram of first stroke using different tribological systems and heat treatment condition T6 (a) and severity of chevron cracking depending on friction (b).

As can be seen in Fig. 4 (b), the severity of the chevron cracking varied regarding the TS. A dependency of chevron cracking and punch force can be postulated since the characteristics of the chevron cracks became more distinctive with lower punch force F, as the hydrostatic stress in the center of the workpiece was reduced with lower friction [5], although there were exceptions from this rule. The GR treated specimen had less critical chevron cracks during this study. In the lubricated state, the punch forces were lower than under dry conditions. While using S3, a MHP surface finish in the lubricated state decreased the punch force compared to a HPPMS surface finish. This can be explained by the formation of lubricant pockets, which lead to reduced friction behavior. Although with S1 and S2, this effect was reversed. On this account, hydrodynamic and hydrostatic effects could occur, which decreased friction and therefore the punch force. On the contrary, the very homogenous surface of the HPPMS process seemed not to grant hydrodynamic effects. As a result, the lubricant effect E_B was lower when using HPPMS-finished surfaces.

Table 2 summarizes the results of the evaluation using DoE. All the effects shown were calculated with the ground die (A- setting) and no lubrication (B- setting) as a reference. HPPMS or MHP were used as the A+ setting, and S1, S2 or S3 as the B+ setting. For each effect calculation,

all possible combinations of the *plus* and *minus* settings of A and B were considered. The effects of all combinations of the parameter settings A and B were calculated in comparison to the reference state. The effect of each factor was calculated as the difference between the average maximum force F_{max} in the experiments when the factor had the *plus* setting and the average maximum force F_{max} when the factor had the *minus* setting. As an example, the effect E_A was calculated by

$$E_A = \frac{F_{max,A+,B+} + F_{max,A+,B-}}{2} - \frac{F_{max,A-,B+} + F_{max,A-,B-}}{2} \quad (1)$$

For the calculation of effect E_{AB}, the setting of AB is given by the multiplication of the settings of factors A and B. So, for the combination of settings A- and B- or A+ and B+, the AB+ setting would be assumed, whereas for A+ and B- or A- and B+, AB- would be assumed. The effects in dependency of the *plus* or *minus* setting of the other factor were calculated as follows:

$$E_{A(B\overset{+}{-})} = E_A \overset{+}{-} E_{AB}. \quad (2)$$

As the force for the forming process does not significantly change between the experiments, the effects can be mostly explained by increased or decreased friction behavior. Regarding the main effects, the results indicate that the use of lubricants had a positive effect E_A on the maximum punch force F_{max} independently of the die treatment. The MHP treated die, on the other hand, showed a negative effect E_B on the maximum punch force F_{max}, while the HPPMS treated die had a positive effect E_B on the maximum punch force F_{max}. Considering the main effects E, the HPPMS treated die showed a positive effect $E_{A(B-)}$ on the maximum punch force F_{max} when dry pressing. The MHP treated die had the opposite effect $E_{A(B-)}$ and showed a negative effect on the maximum punch force F_{max}.

Table 2. DoE effects maximum punch force F_{max} of die treatment (A) and lubricant (B).

Effect E	HPPMS			MHP		
	SS1	SS2	SS3	SS1	SS2	SS3
E_A [kN]	-98.17	-85.65	-62.81	66.61	54.60	47.70
E_B [kN]	-307.92	-268.07	-205.89	-405.65	-390.34	-357.89
$E_{A(B-)}$ [kN]	-148.01	-148.01	-148.01	114.50	114.50	114.50
$E_{A(B+)}$ [kN]	-48.33	-23.28	22.39	18.72	-5.31	-19.10
$E_{B(A-)}$ [kN]	-357.76	-330.43	-291.09	-357.76	-330.43	-291.09
$E_{B(A+)}$ [kN]	-258.07	-205.70	-120.69	-453.54	-450.25	-424.69

Fig. 5 compares the punch force-time-graphs using workpiece material in T6 and soft annealed heat treatment conditions with the ground die and lubricant S1. The test pairing was chosen for further analysis due to its average damage value regarding the severity of chevron cracks. By comparing the two courses, it can be seen that the maximum punch force F was significantly lower when in soft annealed than in T6 condition. Furthermore, the punch force-time-graph of the soft annealed heat treatment condition showed no drop in punch force F but a nearly linear progression after reaching the maximum punch force F_{max}. Moreover, the gradient of the punch force-time-graph for the soft annealed condition was smaller compared to the T6 condition during the rise and

fall of the punch force F during of the process. Using the soft annealed condition, no chevron cracks emerged during pressing. The workpiece was free of defects.

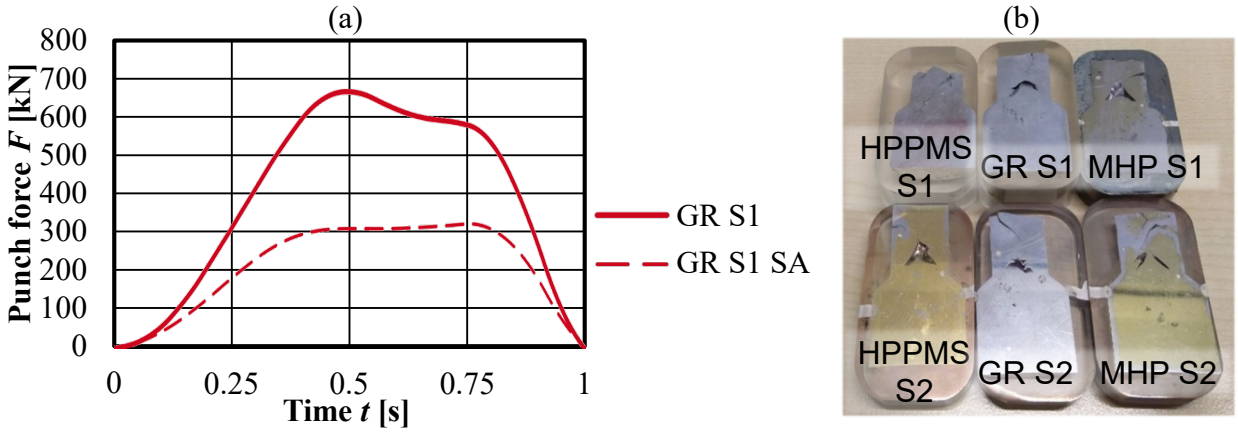

Fig. 5. Punch force-time-diagram of first stroke soft annealed and heat treatment condition T6 (a) and typical chevron crack formation during the experiments (b).

Numerical results.

In order to validate the simulation model, the punch force during FFIE and the geometry of the finished workpiece were compared to the simulation results. Fig. 6 (a) shows this comparison. The simulation was conducted using only the Hensel Spittel parameters [10] of EN AW 7075 in the soft annealed state, as the parameters for the heat treatment condition T6 were not available during this study. Regarding the punch force, the experimental data were comparable to the simulation data using low friction conditions. Both the experimental data and the simulation with low friction conditions reached a similar maximum punch force of about 300 kN. The maximum punch force during the experiments was about 8% higher than the punch force in the low friction simulation. The simulation model with low friction conditions shared a very similar gradient with the experimental data at the beginning of the FFIE process. The key difference was the negative force gradient at the end of the process, which decreased slower in the experimental data, which was the result of the reduced punch velocity at the end of the experiments. Furthermore, the lode parameter as well as triaxiality were investigated in order to evaluate the workpiece damage [9]. The triaxiality η is defined as

$$\eta = \frac{\sqrt{2}\cdot(\sigma_1+\sigma_2+\sigma_3)}{3\cdot\sqrt{(\sigma_1-\sigma_2)^2+(\sigma_1-\sigma_3)^2+(\sigma_2-\sigma_3)^2}} \tag{3}$$

where σ_1, σ_2 and σ_3 are the principal stresses [10]. The Lode parameter $\underline{\theta}$ is described by

$$\underline{\theta} = 1 - \frac{2}{\pi}\cdot arccos\,(\xi) \tag{4}$$

where ξ is the normalized third deviatoric stress invariant [11]. Using the lode parameter, areas of tensile and compressive stress can be identified in a simulation model. Fig. 6 (b) shows that most chevron cracks during the experiments occurred in the areas where areas with high compressive stresses met areas with high tensile stresses. The stress tensor in material flow direction in the center of the peg was characterized by large compressive stress values, while the surrounding area was characterized by large tensile stresses. The tensile stress values on the inside of the peg increased during the process, and lead to material failure in this area, which resulted in the occurrence of a chevron crack. Afterwards, tensile stress values continued to grow until another

chevron crack occured. Chevron cracks and cracks that started at the surface of the peg mostly seemed to grow alongside the areas where tensile and compressive stresses met.

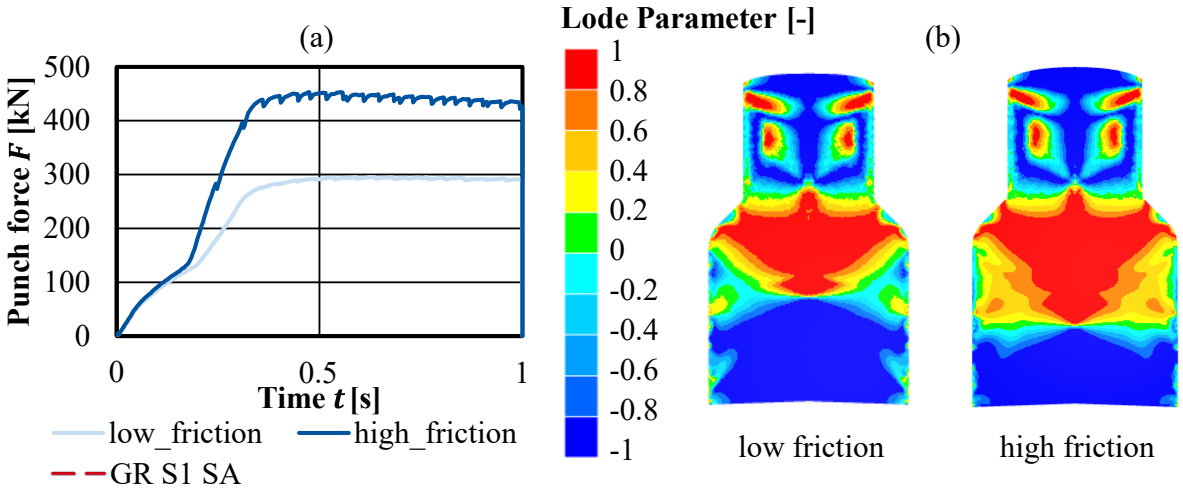

Fig. 6. Punch force over time during simulation (a) and Lode parameter during forming (b).

In Fig. 7 (a), the triaxiality at the end of the forming process is shown. Using both low and high friction conditions, tensile stress could be found near the surface of the peg, while the center was largely influenced by compressive stress. In the center of the extruded shoulder, which coincides with the area where most chevron cracks occurred, sheer stress was dominating and the highest von Mises stress values occurred. Right above this zone, the von Mises stress values decreased significantly, which lead to material failure in this specific area.

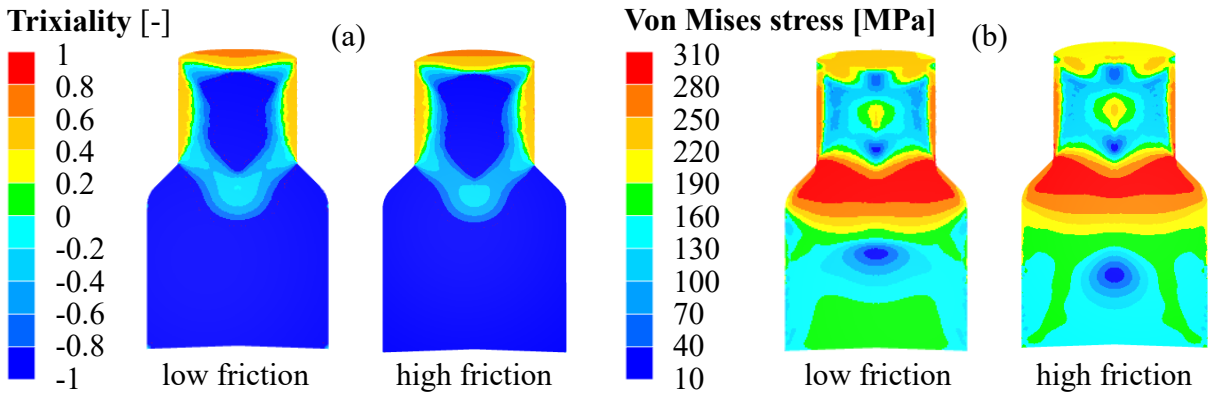

Fig. 7. Triaxiality during forming (a) and von Mises stress during forming (b).

Regarding the simulation of chevron cracks during the FFIE process, simulations in Forge were carried out using the normalized Latham-Cockcroft damage criterion, which is the most commonly used damage criterion in cold forming [12] and has already been proven to be suitable for the analysis of chevron cracks in cold extrusion processes [13]. For cold forming, a critical damage parameter of 0.5 is suggested. No chevron cracks occurred in the experiments that use the process parameters presented in this paper while using specimen in the soft annealed state, which was confirmed by the simulation results. Nevertheless, in order to investigate the growing process of chevron cracks during the forming simulation without changing the material behavior of EN AW 7075, the critical damage parameter was set to 0.2. In this theoretical case, the formation of chevron cracks started early during the FFIE process in the center of the reduction shoulder. Throughout the crack growth, the area between the crack itself and the lateral surface of the

workpiece showed an increased value for the Latham-Cockcroft damage criterion when compared to the rest of the specimen. Once the first chevron crack reached a certain width, another chevron crack occurred in the same area that the first one occurred in. During the experiments, multiple chevron cracks only appeared in a few specimen. On the other hand, the chevron cracks grew larger than in the simulation model, which can be explained by the different heat treatment condition. Furthermore, the resulting damage parameter was largely influenced by the friction conditions used during the simulation. By using high friction parameters, the occurrence of chevron cracks during the FFIE process was significantly reduced, which confirms the experimental results. It should be noted that, unlike in the experiments, the occurrence of chevron cracks during the simulations did not affect the punch force-time-diagram.

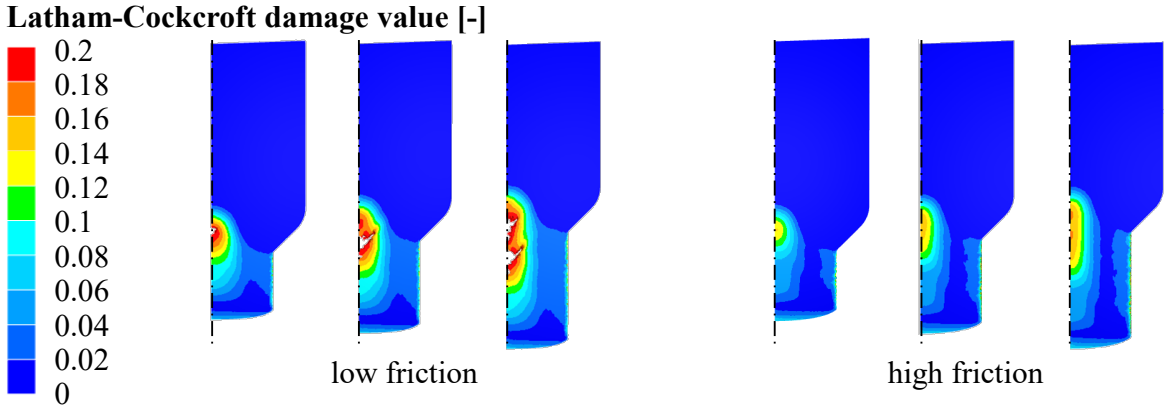

Fig. 8. Latham-Cockcroft damage value during FFIE simulation.

Summary

Within the present study, extensive analyses were carried out to investigate the cause-effect relations between heat treatment condition, damage development and tribological system. For this purpose, FFIE experiments were executed with workpieces made of the aluminum alloy EN AW 7075 in the different heat treatment conditions T6 and soft annealed as well as different tribological systems. The key findings of this study are as follows:

- A dependency between friction and chevron crack characteristics was shown. With increasing maximum punch force $\boldsymbol{F_{max}}$ and thus with increasing friction, the chevron crack characteristics that occurred in heat treatment condition T6 became less distinctive. These findings were also confirmed by the numerical investigations of this study.
- It was shown that the punch force-time-graph at the occurrence of chevron cracks had a different characteristic than that of defect-free components. All courses showed a drop in punch force $\boldsymbol{F}$ in form of a buckling after reaching the maximum force $\boldsymbol{F_{max}}$. This buckling did not occur in other experiments without chevron cracks with the same tool geometry and experimental parameters [13]. The buckling of the curve became increasingly apparent as the chevron cracks became more distinctive and is considered as a result from the sudden stress relief due to bursting of the material.
- The simulation model with low friction showed a mostly similar force curve to the experimental data using the soft annealed state of EN AW 7075. Simulations showed that chevron cracks occur in the areas where high tensile and high compressive stresses met.

Acknowledgment
This work was funded by the Deutsche Forschungsgemeinschaft (DFG, German Research Foundation) – Projektnummer 460819047 (TriboLub).

References
[1] H. Haghighat, A. Parghazeh, An investigation into the effect of strain hardening on the central bursting defects in rod extrusion process, Int. J. Adv. Manuf. Technol. 93 (2017) 1127-1137. https://doi.org/10.1007/s00170-017-0577-6
[2] Volz, H., Kaltmassivumformung: Präzision in Serie, Available online: https://www.massivumformung.de/fileadmin/user_upload/6_Presse_und_Medien/Veroeffentlichungen/Extra-Info/Kaltmassivumformung_Druckversion_12-10-04.pdf. 2017 (accessed 18 November 2022).
[3] C. Buse, Potenziale und Grenzen der Schallemissionsanalyse zur Online-Prozessüberwachung in der Kaltmassivumformung von Stahlwerkstoffen, PhD Thesis, Univ. Hannover, 2017.
[4] C. McVeigh, W.K. Liu, Prediction of central bursting during axisymmetric cold extrusion of a metal alloy containing particles. Int. J. Solid. Struct. 43 (2006) 3088-3105. https://doi.org/10.1016/j.ijsolstr.2005.05.019
[5] G. Dieter, K. Howard, S.L. Semiatin, Handbook of workability and process design, ASM International, 2003.
[6] P. McAllen, P. Phelan, Ductile Fracture by Central Bursts in Drawn 2011 Aluminium Wire, Int. J. Fract. 135 (2005) 19–33. https://doi.org/10.1007/s10704-005-3470-5
[7] B.A. Behrens, S. Hübner, H. Vogt, O. Golovko, S. Behrens, F. Nürnberger, Mechanical properties and formability of EN AW-7075 in cold forming processes, IOP Conf. Ser.: Mater. Sci. Eng. 967 (2020). https://doi.org/10.1088/1757-899X/967/1/012017
[8] J. Antony, Design of Experiments for Engineers and Scientists, Elsevier insights, Elsevier, Amsterdam, 2014. https://doi.org/10.1016/B978-0-08-099417-8.00010-9
[9] A. Hensel, Th. Spittel, Kraft- und Arbeitsbedarf bildsamer Formgebungsverfahren. VEB Deutscher Verlag für Grundstoffindustrie, Leipzig, 1978.
[10] M. Basaran, Stress State Dependent Damage Modeling with a Focus on the Lode Angle Influence, Diss. RWTH Aachen, Shaker, Aachen, 2011.
[11] Y. Bai, T. Wierzbicki, A new model of metal plasticity and fracture with pressure and Lode dependence, Int. J. Plast. 24 (2008) 1071-1096. https://doi.org/10.1016/j.ijplas.2007.09.004
[12] S. Stebunov, A. Vlasov, N. Biba, Prediction of fracture in cold forging with modified Cockcroft-Latham criterion, Procedia Manuf. 15 (2018) 519-526. https://doi.org/10.1016/j.promfg.2018.07.264
[13] J. Choi, H. Lee, Y. Im, A study on chevron crack formation and evolution in a cold extrusion, J. Mech. Sci. Technol. 24 (2010) 1885-1890. https://doi.org/10.1007/s12206-010-0605-z
[14] M. Müller, R. Hild, D. Trauth, T. Bergs, Investigation of different tribological systems during full forward impact extrusion of aluminum alloy EN AW 6082, Industr. Lubric. Tribol. 72 (2019) 709-712. https://doi.org/10.1108/ILT-08-2019-0316